buildings

MDPI

Article

Mechanical Properties of Precast Recycled Concrete Thermal Insulation Panels with GFRP Connectors

Xiuling Li [1,2,*], Haodong Sun [2], Tianxuan Zhang [2], Tongxing Bu [2], Haoming Yu [2], Jiaxin Sun [2] and Hu Feng [3]

[1] School of Civil Engineering, Shandong Jiaotong University, Jinan 250357, China
[2] Key Laboratory of Building Structural Retrofitting and Underground Space Engineering, Ministry of Education, School of Civil Engineering, Shandong Jianzhu University, Jinan 250101, China; horizonsun77@163.com (H.S.)
[3] School of Civil Engineering, Zhengzhou University, Zhengzhou 450001, China; fenghu@zzu.edu.cn
* Correspondence: dlutiem@163.com

Abstract: To improve both the composite performance of precast thermal insulation wall panels and the environmental sustainability of the structure, this study employs recycled concrete, and introduces an innovative four-footstool Glass Fiber Reinforced Plastic (GFRP) connector to join the inner and outer panels of precast thermal insulation wall systems. The experimental program included pull-out, shear, and bending tests to compare the performance of wall panels equipped with traditional Thermomass MS connectors and the novel GFRP connectors, using both conventional and fully recycled concrete. The results indicate that, when paired with recycled concrete, the GFRP connectors exhibited a 14.8% higher pull-out bearing capacity than the traditional connectors. Additionally, shear tests demonstrated that the GFRP connectors offered a 20.6% improvement in shear resistance compared to the Thermomass MS connectors. The bending strength of panels with GFRP connectors also showed an enhancement, with a 16.5% increase in flexural strength relative to those using traditional connectors. Notably, the GFRP connectors contributed to a more uniform crack distribution under loading, thereby improving the overall structural integrity. A reduction factor γ for the GFRP four-footstool connector was proposed based on a fully composite model, and the analysis of the composite degree calculation showed that the recycled concrete sample using the new GFRP connector had the highest composite degree.

Keywords: GFRP connectors; precast structure; recycled concrete; mechanical performance; thermal insulation wall panels

check for updates

Academic Editor: Cedric Payan

Received: 14 February 2025
Revised: 5 March 2025
Accepted: 10 March 2025
Published: 12 March 2025

Citation: Li, X.; Sun, H.; Zhang, T.; Bu, T.; Yu, H.; Sun, J.; Feng, H. Mechanical Properties of Precast Recycled Concrete Thermal Insulation Panels with GFRP Connectors. *Buildings* **2025**, *15*, 891. https://doi.org/10.3390/buildings15060891

Copyright: © 2025 by the authors. Licensee MDPI, Basel, Switzerland. This article is an open access article distributed under the terms and conditions of the Creative Commons Attribution (CC BY) license (https://creativecommons.org/licenses/by/4.0/).

1. Introduction

In the context of sustainable architecture and energy-efficient design, prefabricated insulated exterior wall panels have gained increasing attention due to their superior thermal insulation properties, ease of construction, and environmental benefits [1–3]. Compared to traditional cast-in-place walls, prefabricated concrete sandwich panels significantly reduce construction time, minimize on-site wet work, lower construction risks, and enhance overall efficiency. These panels have become a core element in modern energy-efficient building systems, effectively reducing building energy consumption and improving overall sustainability [4–6].

Recently, the popularity of prefabricated insulated wall panels has risen due to their energy efficiency and construction advantages. However, traditional systems using connectors, such as the Thermomass MS needle-type connector, may have limitations that

hinder their overall performance. These limitations include poor load transfer efficiency, particularly at the interface between the concrete wythes and the insulation layer, as well as susceptibility to stress concentrations [7–9]. The relatively small contact area between the connector and the concrete can lead to uneven load distribution, resulting in localized failures and reduced durability over time [10,11]. Additionally, traditional connectors often fail to ensure optimal composite action between the concrete and insulation, compromising the overall structural integrity of the wall panel [12,13]. These shortcomings highlight the need for improved connectors to enhance the performance and longevity of prefabricated insulated wall panels [14,15]. In particular, at the interface between the two concrete layers, composite behavior can lead to uneven mechanical performance distribution, affecting both load-bearing capacity and durability. The degree of composite action in sandwich panels depends on the shear connector configuration and the connection method used [16,17]. Effective connectors are crucial to ensuring the stability, durability, and energy performance of the interface between the insulation material and the concrete structure [18–21]. Therefore, developing connectors that meet structural and energy efficiency requirements is vital for advancing this field.

For instance, Wang et al. [22] proposed an innovative GFRP shell panel and studied the effects of mesh thickness, mesh spacing, mesh height, and skin thickness on axial stiffness, displacement ductility, and energy dissipation. They developed corresponding models to predict the strength of this type of wall panel. Choi et al. [23] performed monotonic loading and wind-induced cyclic loading tests on full-scale wall panels, demonstrating that all specimens met the usage standards. Benayoune et al. [24] examined the structural performance of precast concrete sandwich panels (PCSP) under bending, using both experimental and theoretical methods, and proposed a two-dimensional finite element model to assess the composite action in the PCSP system. Sharaf et al. [25] investigated a novel sandwich panel with two GFRP shells laminated onto the exterior of a prefabricated polyurethane foam core. Their results show that panels with soft cores were vulnerable to local effects under concentrated loads, experiencing inward wrinkling of the compressed surface at lower ultimate loads. Zhi et al. [26] introduced a new type of shear connector made from steel and GFRP materials. They conducted flexural tests on 12 full-scale precast concrete sandwich panels to assess their composite behavior. Naito et al. [27] examined 14 different shear connector types, quantified their failure modes, and established simplified multilinear strength curves for each type. Kang et al. [28] proposed a design model for sandwich wall panels (SWPs) reinforced with GFRP grids to predict flexural failure, simplifying the calculation process for such structures.

In the design of PCSP, composite action refers to the interaction between the two concrete wythes and the intermediate insulation layer in the sandwich panel. Based on the degree of composite effect, PCSPs can be classified into three design types: non-composite (NC), partially composite (PC), and fully composite (FC) [29,30]. The degree of composite action between the two concrete interlayers is critical for determining the mechanical properties, bearing capacity, and stiffness of the panel. The composite effect depends on the connectors, which enable the concrete and insulation layers to collaboratively bear external loads. Stronger composite effects lead to better collaboration between the layers, thereby improving strength and stiffness [31–33]. Although many connectors only provide partial composite effects, advanced connectors, such as high-strength steel or fiberglass-reinforced plastic, can significantly improve performance, reduce material use, and lower long-term construction and maintenance costs [34,35].

To address the limitations of existing connectors, this study proposes a novel four-footstool GFRP connector. Made from GFRP material, this connector exhibits high strength, low thermal conductivity, and excellent corrosion resistance, contributing to

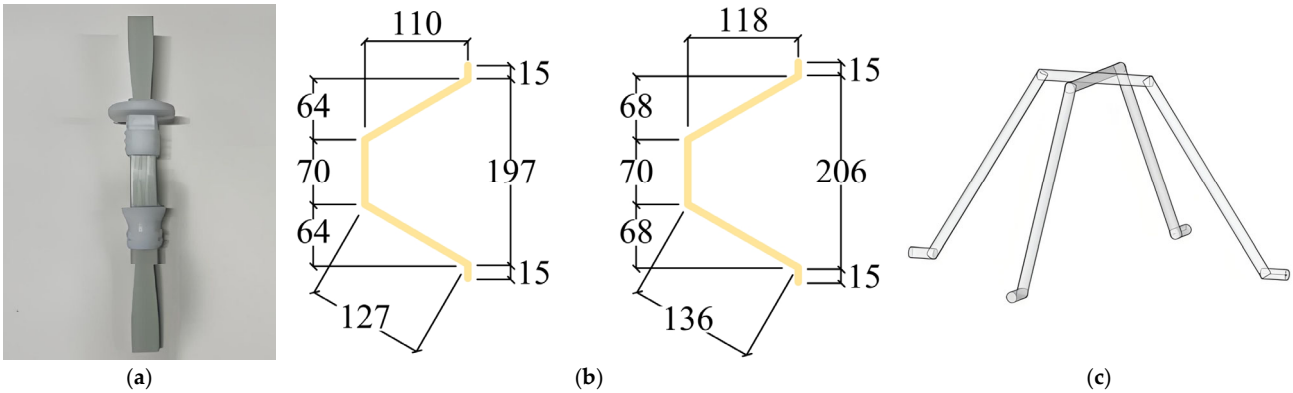
improved thermal insulation performance. Compared to the conventional Thermomass MS needle-type connector, the four-footstool connector increases the contact area with the concrete wall panel, thereby enhancing mechanical performance. Manufactured from epoxy resin-based GFRP, this new connector offers greater durability and efficiency than traditional connectors.

To evaluate the performance of the newly designed connector, this study conducted pull-out, shear, and flexural tests to compare the mechanical properties of the four-footstool GFRP connector with those of the conventional Thermomass MS needle-type connector. The primary focus was on analyzing the load–displacement behavior, ultimate strength, and failure modes of the two connector types under different concrete materials (C35 and recycled concrete). The experimental results are expected to provide deeper insights into the advantages of the novel connector in terms of structural performance, offering theoretical support for optimizing prefabricated insulated wall panel systems. Finally, through theoretical analysis, this study calculates the degree of composite action in wall panels using the new connector, and proposes a modification coefficient for the flexural strength calculation of external wall panels with the GFRP four-footstool connector. The introduction of this modification coefficient, γ, was validated by experimental testing, where the adjusted flexural strength using γ closely matched the experimentally measured values. This adjustment factor simplifies the design process, as engineers can apply the coefficient to the traditional flexural strength formula to account for the improved composite action due to the GFRP four-footstool connectors.

2. Experimental Program

2.1. Design of Connectors

Currently, most connectors used in industrial production for wall panels are Thermomass MS needle-type connectors, as shown in Figure 1a. These connectors, made from glass fiber, offer advantages such as high strength, excellent corrosion resistance, and low thermal conductivity. However, they have certain limitations in composite performance. The main issue lies in the relatively small contact area between the connector and the concrete layers, which can lead to inefficient load transfer and stress concentration at the interface between the concrete wythes and the insulation layer. This can result in suboptimal composite action and a higher likelihood of localized failure.



(**a**) (**b**) (**c**)

Figure 1. Design of connectors: (**a**) Thermomass MS needle type connector; (**b**) GFRP four-footstool connector design drawing; (**c**) GFRP four-footstool connector combination diagram.

To overcome these limitations, a novel GFRP four-footstool connector was designed, as shown in Figure 1b. The four-footstool connector is formed by the cross-combination of two similar open trapezoidal connectors, with the assembled configuration illustrated in Figure 1c. This cross-combination design significantly increases the contact area between

the concrete layers and the insulation, improving load transfer and ensuring better stress distribution. By increasing the effective contact area, the GFRP four-footstool connector enhances the composite action between the two concrete layers and the insulation, which leads to improved load-bearing capacity and overall structural performance. The four-footstool connector can effectively distribute the load and avoid excessive material usage while ensuring the required strength and stability. Additionally, the unique four-footstool geometry provides better mechanical interlocking between the concrete and insulation layers. The combination of two trapezoidal shapes helps to optimize the connection, providing a more robust and stable composite structure. This design minimizes the risk of failure at the connector interface and addresses the composite performance shortcomings of the Thermomass MS needle-type connectors, making the GFRP four-footstool connector a more efficient and reliable choice for precast insulated wall panels.

The GFRP four-footstool connector is entirely made of epoxy resin-based GFRP material, with a cylindrical diameter of 8 mm. The initial 8 mm diameter of the GFRP four-footstool connector was chosen based on practical design considerations and typical connector sizes. However, further testing with larger diameters (e.g., 10 mm, 12 mm, 14 mm) will be conducted to assess their impact on the mechanical performance of the connector, the load-bearing capacity, and the overall efficiency. It is manufactured through thermoplastic processing using custom factory molds. The molds and finished products are shown in Figure 2.



(**a**) (**b**)

Figure 2. Connector mold and finished product: (**a**) GFRP four-footstool connector mold; (**b**) GFRP four-footstool connector.

2.2. Design of Specimens

A total of four groups of comparative pull-out tests were designed for the connectors of prefabricated thermal insulation exterior wall panels. One specimen was fabricated and tested for each group, with variables including concrete materials (ordinary concrete and fully recycled concrete) and connector types (Thermomass MS needle type connectors and GFRP four-footstool connectors). The anchor lengths at both ends of the Thermomass MS needle type connectors were 35 mm, while the internal and external anchor lengths of the GFRP four-footstool connectors were 34 mm, which is essentially consistent with the Thermomass MS type. The thickness of the insulation layer used in the tests was 50 mm for all specimens. The specimen numbers and specific parameters are listed in Table 1. One specimen was designed for each group of tests. The dimensions and reinforcement of the specimens are shown in Figure 3.

A total of four groups of comparative shear tests were designed for the connectors of prefabricated thermal insulation exterior wall panels. The dimensions, materials, and anchorage lengths of the two types of connectors were consistent with those used in the pull-out tests. The specimen numbers and specific parameters are listed in Table 2. The specimen design is shown in Figure 4.

Table 1. Parameters of pull-out test.

Specimen	Connector Type	Exterior Panel Material	Interior Panel Material
POG-C [1]	GFRP Four-Footstool	C35	C35
POG-R [2]	GFRP Four-Footstool	RC	RC
POT-C [3]	Thermomass MS	C35	C35
POT-R [4]	Thermomass MS	RC	RC

[1] "POG-C" is pull-out GFRP four-footstool connector-C35. [2] "POG-R" is pull-out GFRP four-footstool connector—recycled concrete. [3] "POT-C" is pull-out Thermomass connector—C35. [4] "POT-R" is pull-out Thermomass connector—recycled concrete.

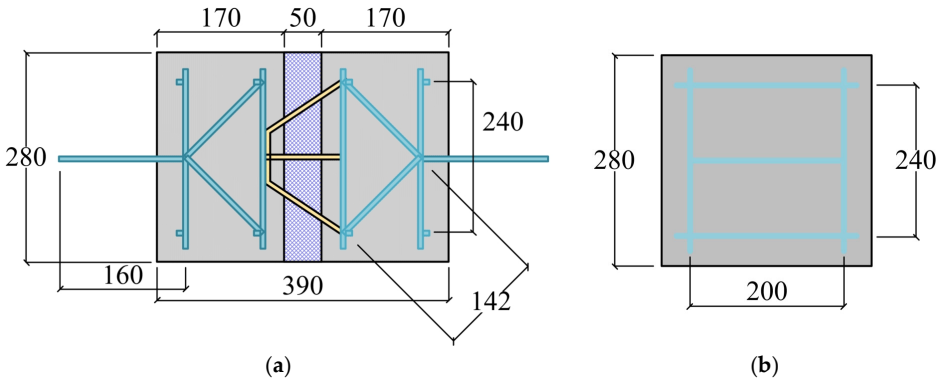


Figure 3. Construction design of pull-out specimen: (**a**) front view; (**b**) top view.

Table 2. Design parameters of shear test.

Specimen	Connector Type	Inner and Outer Panel Materials
CG-C [1]	GFRP four-footstool	C35
CG-R [2]	GFRP four-footstool	RC
CT-C [3]	Thermomass MS	C35
CT-R [4]	Thermomass MS	RC

[1] "CG-C" is cut-GFRP four-footstool connector—C35. [2] "CG-R" is cut-GFRP four-footstool connector—recycled concrete. [3] "CT-C" is cut-Thermomass connector—C35. [4] "CT-R" is cut-Thermomass connector—recycled concrete.

Flexural test specimens of prefabricated insulated exterior wall hanging panels were designed and fabricated. The comparison parameters included the following: W-1 (C35 specimen with Thermomass MS needle type connector) and W-2 (C35 specimen with GFRP four-footstool connector); W-2 (using ordinary concrete) and W-4 (using fully recycled concrete). Both specimens used GFRP four-footstool connectors. W-3 and W-4 had the same concrete materials and connectors. W-3 (the insulation board was in the middle of the wall panel, and the thickness of the inner and outer wall panels was the same), W-4 (the outer wall thickness was 50 mm, and the inner wall thickness was 80 mm). The specific design parameters are shown in Table 3.

A total of four flexural test specimens were fabricated. The size of the specimens was 3200 mm × 1200 mm × 180 mm. The thickness of the inner and outer wall panels and the locations of the insulation boards of W-1, W-2 and W-4 were the same, with the thickness from the inside to the outside being 80 mm, 50 mm, and 50 mm, respectively. The thickness of W-3 from the inside to the outside was 65 mm, 50 mm, and 65 mm. W-1 used ordinary concrete with a Thermomass MS needle-type connector, W-2 used C35 with a GFRP four-footstool connector, and W-3 and W-4 both used fully recycled concrete with a GFRP four-footstool connector.

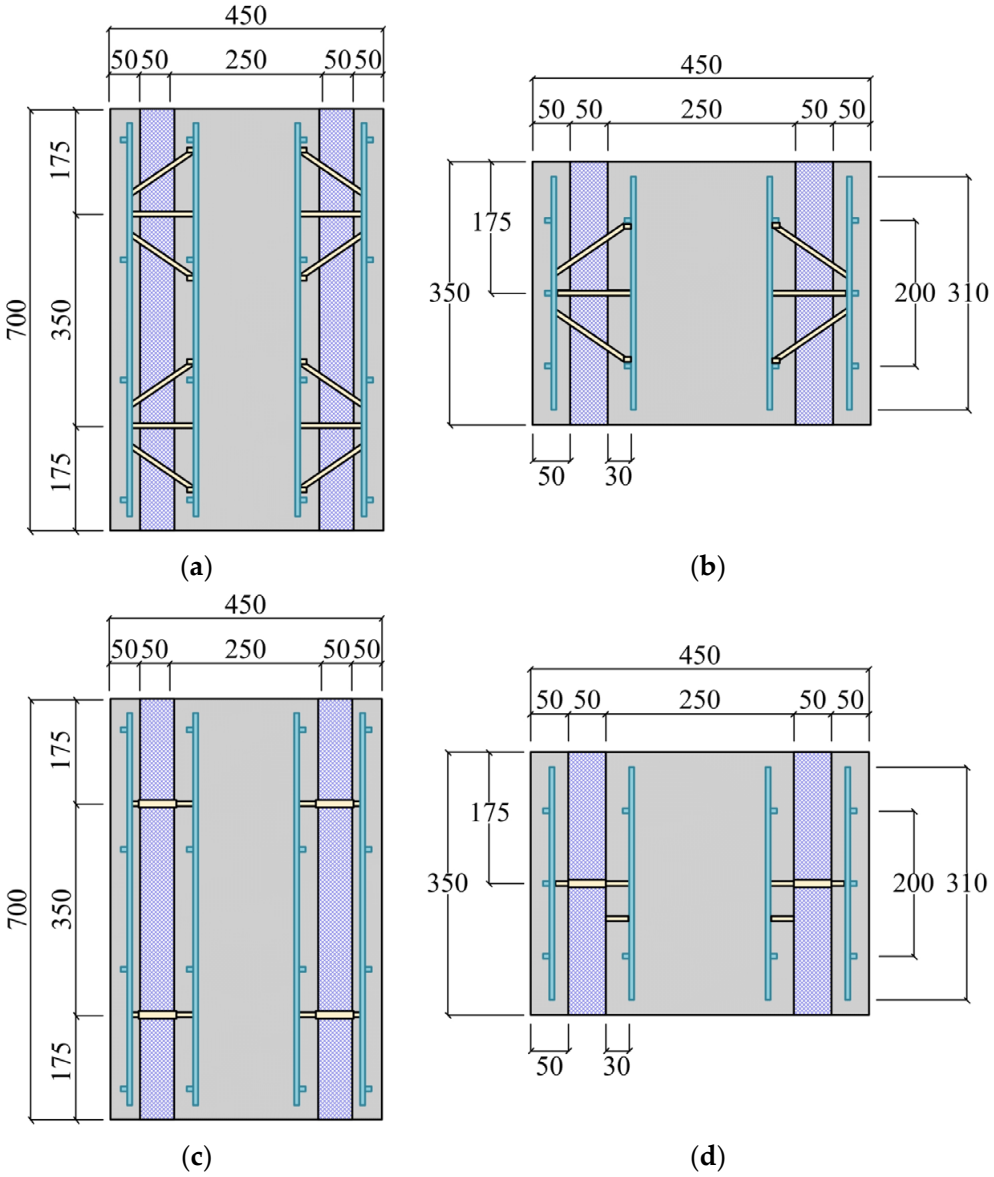


Figure 4. Construction design of shear specimen: (**a**) main view of GFRP specimen; (**b**) top view of GFRP specimen; (**c**) main view of Thermomass specimen; (**d**) top view of Thermomass specimen.

Table 3. Design parameter of flexural specimen of wall panels.

Specimen	Outer Panel/mm	Inner Panel/mm	Connector	Outer Material	Inner Material
W-1 [1]	50	80	Thermomass MS Type	C35	C35
W-2	50	80	GFRP Four-footstool	C35	C35
W-3	65	65	GFRP Four-footstool	RC	RC
W-4	50	80	GFRP Four-footstool	RC	RC

[1]. "W-1" is wall 1.

Both the inner and outer wall panels of the specimen were equipped with a single-layer steel mesh of Φ8@200. The connectors were evenly distributed at a spacing of 350 mm × 250 mm longitudinally and transversely. The specific dimensions and reinforcement diagram of the sample are shown in Figure 5.

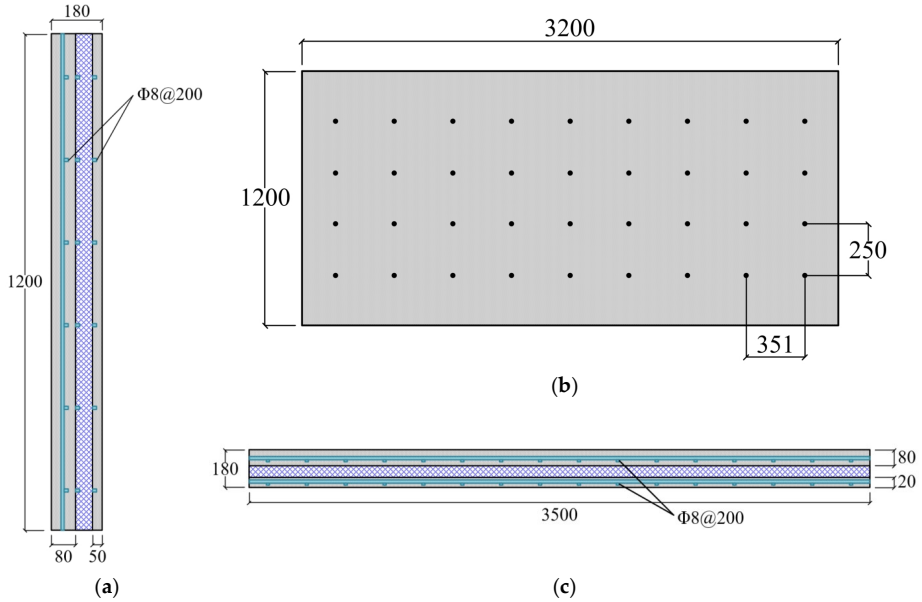


Figure 5. Construction design of flexural specimen: (**a**) side view; (**b**) top view; (**c**) front view.

2.3. Materials

To investigate the mechanical properties and thermal conductivity of fully recycled concrete, and to determine the appropriate mix proportion for the test, an orthogonal experiment was conducted, as shown in Table 4. The factors considered included the water–cement ratio, RCA replacement rate, RFA replacement rate, RCP replacement rate, and the amount of AOS air-entraining agent. A total of 16 test groups were established. The dosage of the water-reducing agent was determined based on the fluidity of the mix. The base mix used for the test was ordinary C35 concrete, as shown in Table 5. In the experiment, RCP was used to replace a portion of the cement in the base mix according to the design ratio, while the water-reducing agent and AOS air-entraining agent were added based on the mass of the cementitious materials (cement and RCP) in the mix, in accordance with the design specifications.

Table 4. Mix proportion design of orthogonal test.

Mixture	w/b [1]	RCA [2] Replacement Rate (%)	RFA [3] Replacement Rate (%)	RCP [4] Replacement Rate (%)	AOS Air-Entraining Agent [5] (%)
1	0.38	0	0	0	0
2	0.38	25	25	15	0.07
3	0.38	50	50	30	0.14
4	0.38	75	75	45	0.21
5	0.43	0	25	30	0.21
6	0.43	25	0	45	0.14
7	0.43	50	75	0	0.07
8	0.43	75	50	15	0
9	0.48	0	50	45	0.07
10	0.48	25	75	30	0
11	0.48	50	0	15	0.21
12	0.48	75	25	0	0.14
13	0.53	0	75	15	0.14
14	0.53	25	50	0	0.21
15	0.53	50	25	45	0
16	0.53	75	0	30	0.07

[1] "w/b" is water to binder ratio. [2] "RCA" is recycled concrete aggregate. [3] "RFA" is recycled fine aggregate. [4] "RCP" is recycled concrete powder. [5] "AOS air-entraining agent" is the amount of Alpha–Olefin sulfonate air-entraining agent.

Table 5. Mix proportion of C35 (kg/m^3).

Grade	Cement	NFA [1]	NCA [2]	Water	HRWR [3]
C35	440	700	1050	167.2	4.4

[1] "NFA" is natural fine aggregate. [2] "NCA" is natural coarse aggregate. [3] "HRWR" is a high-range water reducer used to improve the flow ability of concrete.

The compressive and flexural strength tests of fully recycled concrete were conducted as shown in Figure 6a,b. The specimens were placed on a universal testing machine and subjected to uniform loading during the test. At the conclusion of the test, the average strength of each group was recorded for comparison. Thermal conductivity tests were performed using a Hot Disk TPS2500S apparatus (Hot Disk Co., Ltd, Uppsala, Sweden). Prior to testing, the specimens were dried to constant weight in an oven at 80 °C. The probes were clamped using two test specimens to ensure the surfaces were flat, and the contact area was more than twice the size of the test probes. During the testing process, a constant current induced a temperature change, and the resistance change inside the probe caused a voltage drop. The data variation was recorded to accurately measure the thermal conductivity of the sample. The Hot Disk TPS2500S instrument is shown in Figure 6c.



(**a**) (**b**) (**c**)

Figure 6. Recycled concrete properties test: (**a**) Compressive strength test; (**b**) flexural strength tests; (**c**) Hot Disk TPS2500S thermal conductivity meter.

The compressive strength, flexural strength, thermal conductivity and specific heat capacity of 16 groups of test blocks were tested, respectively, and the test results are shown in Table 6. Figure 7 shows the effects of different factors on recycled concrete.

Table 6. Test results.

Mixture	Compressive Strength/MPa	Flexural Strength/MPa	Compression Ratio	Thermal Conductivity/W/m·K	Specific Heat Capacity/MJ/m^3·K
1	66.4	5.9	0.0889	1.2577	0.9814
2	29.6	4.1	0.1385	0.8152	0.4754
3	19.8	2.5	0.1263	0.7505	0.7922
4	16.9	3.2	0.1893	0.6402	0.7332
5	24.0	3.2	0.1333	0.9097	0.5927
6	19.5	3.0	0.1538	1.3423	1.2899
7	17.3	3.2	0.1850	0.6486	0.6028
8	45.8	4.6	0.1004	0.9844	0.8807
9	15.0	2.4	0.1600	0.6854	0.4811
10	33.5	4.4	0.1313	1.4563	1.3870
11	14.1	2.5	0.1773	0.6966	0.3978
12	17.9	3.2	0.1788	0.6860	0.5743
13	15.1	2.5	0.1656	0.5447	0.4738
14	18.4	2.7	0.1467	1.1039	0.9031
15	18.2	3.0	0.1648	0.7356	0.9177
16	17.2	2.4	0.1395	1.2613	1.0015

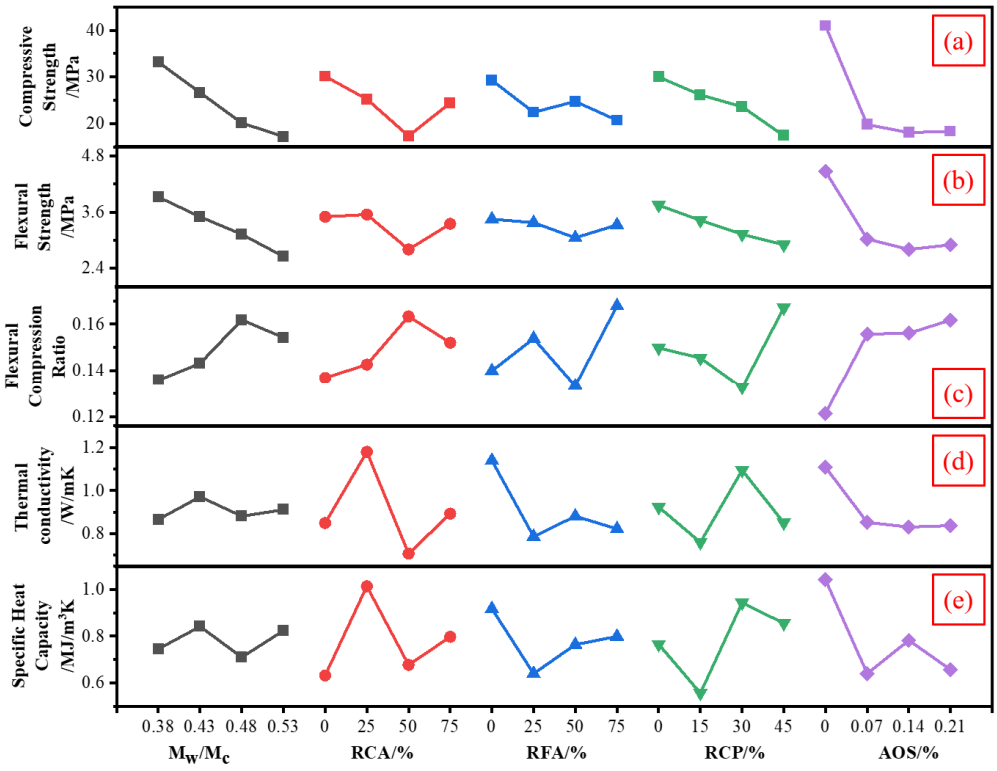


Figure 7. Effects of different factors on recycled concrete: (**a**) Compressive strength; (**b**) flexural strength; (**c**) flexural compression ratio; (**d**) thermal conductivity; (**e**) specific heat capacity.

We used Minitab (v19.1) software on the whole recycled concrete compressive strength, flexural strength and thermal conductivity coefficients of the three mechanical properties and thermal conductivity of the important indicators of the results of the comprehensive analysis. Table 7 shows the results of an analysis of the polarity of the factors, ranking the comprehensive performance of the whole recycled concrete in the order of precedence as regards the impacts of different factors as follows: AOS air-entraining agent > water to binder ratio > RCA replacement rate > RCP replacement rate > RFA replacement rate.

Table 7. Comprehensive performance range analysis.

	w/b [1]	RCA [2] Replacement Rate (%)	RFA [3] Replacement Rate (%)	RCP [4] Replacement Rate (%)	AOS Air-Entraining Agent [5] (%)
Average K1	12.655	11.491	11.296	11.558	15.52
Average K1	10.374	9.993	8.862	10.112	7.884
Average K1	8.044	6.953	9.56	9.281	7.235
Average K1	6.929	9.564	8.282	7.05	7.363
Range	5.727	4.539	3.014	4.508	8.284
Rank	2	3	5	4	1

[1] w/b: water to binder ratio. [2] RCA: recycled concrete aggregate. [3] RFA: recycled fine aggregate. [4] RCP: recycled concrete powder. [5] AOS air-entraining agent: the amount of Alpha–Olefin Sulfonate air-entraining agent.

Through polar analysis and a comprehensive evaluation of the actual conditions, the optimal mix design for fully recycled concrete was determined using an orthogonal test based on the analysis of eight ratio groups. The selected mix design includes a water–cement ratio of 0.43, a recycled concrete aggregate (RCA) replacement rate of 75%, an RCA replacement rate of 50%, a recycled concrete powder (RCP) replacement rate of 15%, and AOS dosage of 0%. Table 8 illustrates the mix proportions for recycled concrete. The compressive strength of the fully recycled concrete prepared using this mix design reaches 45.8 MPa, with a flexural strength of 4.6 MPa and a thermal conductivity of 0.9844,

which is 21.7% lower than that of ordinary concrete. These mechanical properties meet the requirements of most projects, while maximizing the use of recycled materials, thereby contributing positively to the reduction in carbon emissions.

Table 8. Mix proportion of recycled concrete (kg/m^3).

Grade	Cement	RCP [1]	Sand	RFA [2]	Aggregate	RCA [3]	Water	HRWR [4]
RC	374	66	350	350	262.5	787.5	189.2	4.4

[1] "RCP" is recycled concrete powder. [2] "RFA" is recycled fine aggregate. [3] "RCA" is recycled concrete aggregate. [4] "HRWR" is a high-range water reducer used to improve the flow ability of concrete.

2.4. Preparation of Specimens

The production of shear test specimens first involves cutting the insulation board into a rectangular shape of 350 mm × 700 mm, dividing it into two squares and positioning the midpoint, and opening holes to install connectors (Figure 8a). Next, make the specimen mold (Figure 8b), pour vertically, arrange the steel mesh, and place the insulation board, connectors, and steel mesh in order (Figure 8c). Subsequently, C35 concrete and fully recycled concrete are mixed and poured (Figure 8d), compacted and smoothed, and finally covered with plastic wrap for 28 days of natural curing. At the same time, cubic test blocks are made for strength testing.



(**a**) (**b**) (**c**) (**d**)

Figure 8. Production process of shear specimen: (**a**) positioning and installation of connectors; (**b**) sample mold production; (**c**) place insulation board steel mesh; (**d**) concreting.

The size of the insulation board used in the flexural test is 1200 mm × 600 mm, and a single piece cannot cover the entire exterior wall hanging board, so it needs to be spliced. The splicing quality, including the alignment and bonding strength of the insulation boards, was critical for ensuring effective composite action. Any misalignment or weakness in the splicing process could lead to localized load transfer inefficiencies and affect the overall bending performance. Additionally, the GFRP four-footstool connectors were installed at specific locations in the panel. The installation of these connectors required precise alignment and secure placement to ensure optimal load transfer between the concrete and insulation layers. Improper installation could have led to poor mechanical interlocking, diminishing the overall composite behavior and impacting the bending strength of the panel. Both factors—the splicing of the insulation and the installation of the GFRP connectors—were carefully controlled to assess their impacts on the flexural performance of the wall panels.

Firstly, locate the position of the connector according to the design drawings, slot and insert the GFRP four-footstool type connector to ensure its height is consistent with the design, and fix it with epoxy resin adhesive. The test piece is poured horizontally

in layers, and a wooden mold with dimensions of 3200 mm × 1200 mm × 180 mm is made. The inner wall panel concrete is poured and compacted first, and then the insulation board for installing the connectors is laid in sequence to ensure that the connectors are inserted into the concrete. Next, the steel mesh of the exterior wall panel is erected on the connecting pieces, and the concrete pouring of the exterior wall panel is completed before being compacted by vibration. Finally, the surface is smoothed and cured for 28 days. The entire construction process is shown in Figure 9.

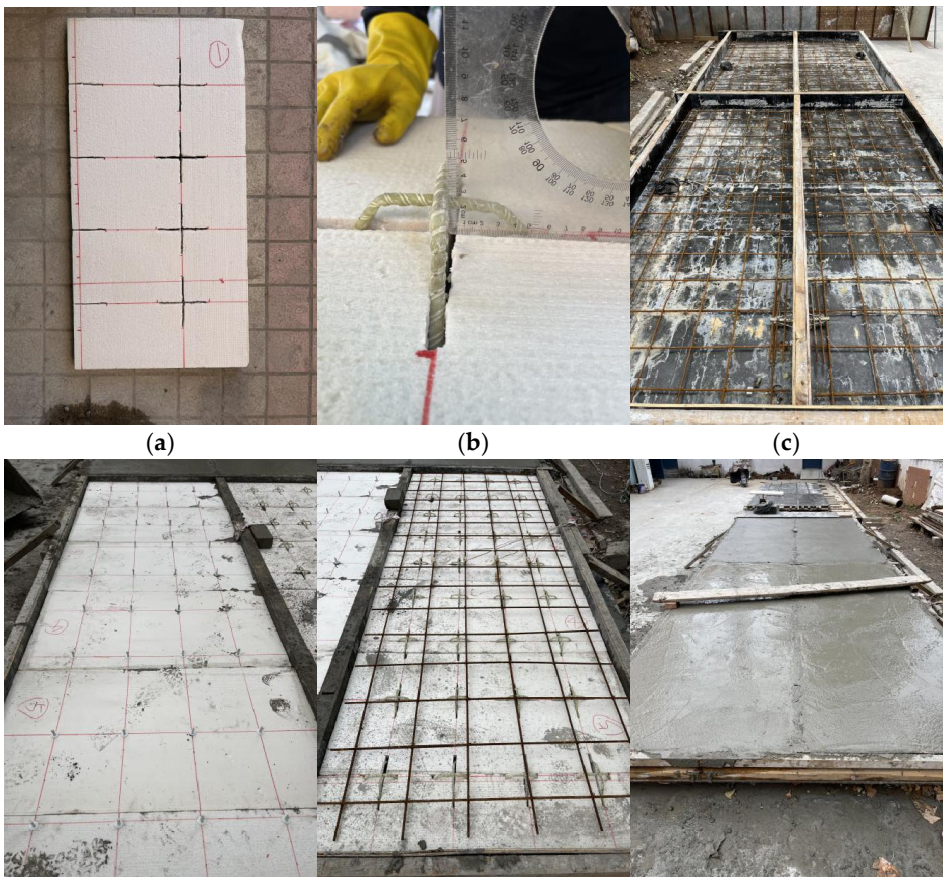


Figure 9. Production process of flexural specimen: (**a**) Insulation board number positioning slotting; (**b**) installation of connectors; (**c**) template production and steel mesh installation; (**d**) installation of connectors and insulation boards; (**e**) laying of outer steel mesh; (**f**) smearing and finishing.

2.5. Test Setup

The pull-out tests were carried out using a microcomputer controlled electro-hydraulic servo universal testing machine model SANS SHT4106 (MTS Industrial Systems (China) Co., Ltd., Shenzhen, China). The specific loading device is shown in Figure 10a,b. During the test, the protruding bars at both ends of the specimen were clamped by the upper and lower clamps of the testing machine. The upper crossbeam of the testing machine was kept fixed and the lower crossbeam was moved downward to generate the tension force. The tests were performed using the displacement-controlled unidirectional loading method. Based on previous studies and experimental considerations, a displacement-controlled loading rate of 0.2 mm/min was selected for the bending tests until the failure of the specimen to ensure the accurate measurement of specimen deformation and to avoid dynamic effects. This rate provided a slow enough load increase to ensure that critical damage characteristics were captured while maintaining a controlled test duration.

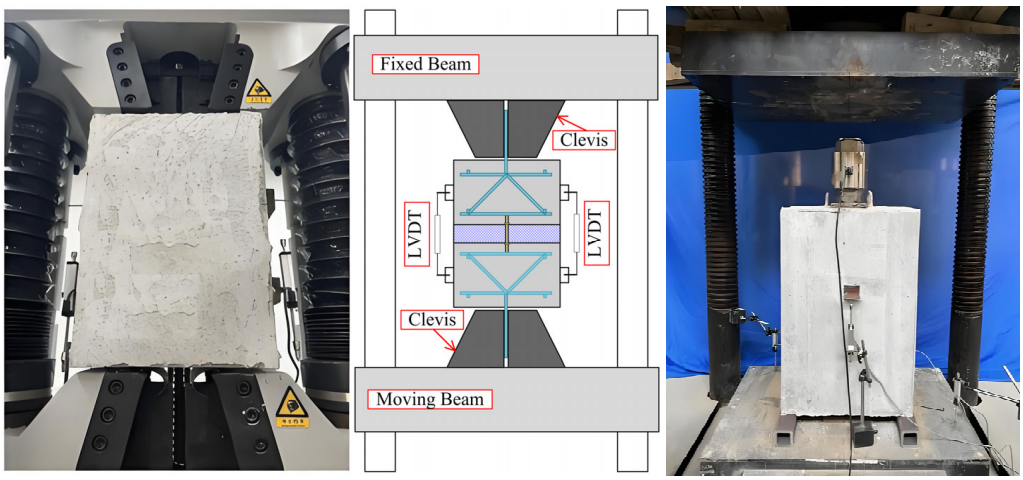


Figure 10. Test setup: (**a**) pull-out test; (**b**) measurement diagram; (**c**) shear test.

The shear tests were conducted using a 500 T pressure testing machine (MTS Industrial Systems (China) Co., Ltd., Shenzhen, China). The specific loading setup is shown in Figure 10c. Two square steel tubes (60 mm × 60 mm × 10 mm) were placed under the bottom of the exterior wall panels as supports, lifting the exterior wall panels on both sides. During the test, the central interior wall panel was subjected to force, and the lifted portion provided sufficient downward displacement space. The loading trolley applied a constant loading speed of 2 mm/min until the load dropped to 85% of the peak value, at which point the specimen was declared failed, and the test ended.

The flexural test employs a four-point support system with symmetrical two-point loading. This method was selected because it ensures a uniform load distribution, creating a well-defined region of pure bending within the panel. To conduct the test, two I-shaped steel beams, with dimensions matching those of the sample, are placed 600 mm apart, positioned symmetrically on both sides at the midpoint of the specimen. A layer of fine sand is applied to the contact surface between the steel beams and the specimen to ensure uniform contact. A distribution beam is placed horizontally at the center between the two steel beams. At the center of the distribution beam, a pressure sensor and a manual hydraulic jack are positioned for loading, as shown in Figure 11.

The specimen is subjected to monotonic loading controlled by the applied load, with the grading monitored via the pressure sensor display. This monotonic loading method was chosen to progressively increase the load until failure, providing clear data on the ultimate flexural strength of panels, failure modes, and deformation characteristics. Before formal testing, a preload of 5 kN is applied to ensure uniform contact between the specimen and the test apparatus, and to verify that the instrument readings are accurate. After this, the load is reduced to zero, and formal testing begins. During formal testing, the load is incremented in 2 kN steps, with each step held for 5 min. This increment size was selected to provide a clear measurement of the response of specimen to loading without unnecessarily extending the testing duration. Although smaller increments could provide more detailed data, the 2 kN step size offered sufficient resolution to capture key behavioral changes in the specimen. Testing continues until the load of specimen drops below 85% of the peak value without recovery, or until the deflection reaches 1/50 of the plate span length. At this point, the specimen is considered damaged, and the test is terminated.

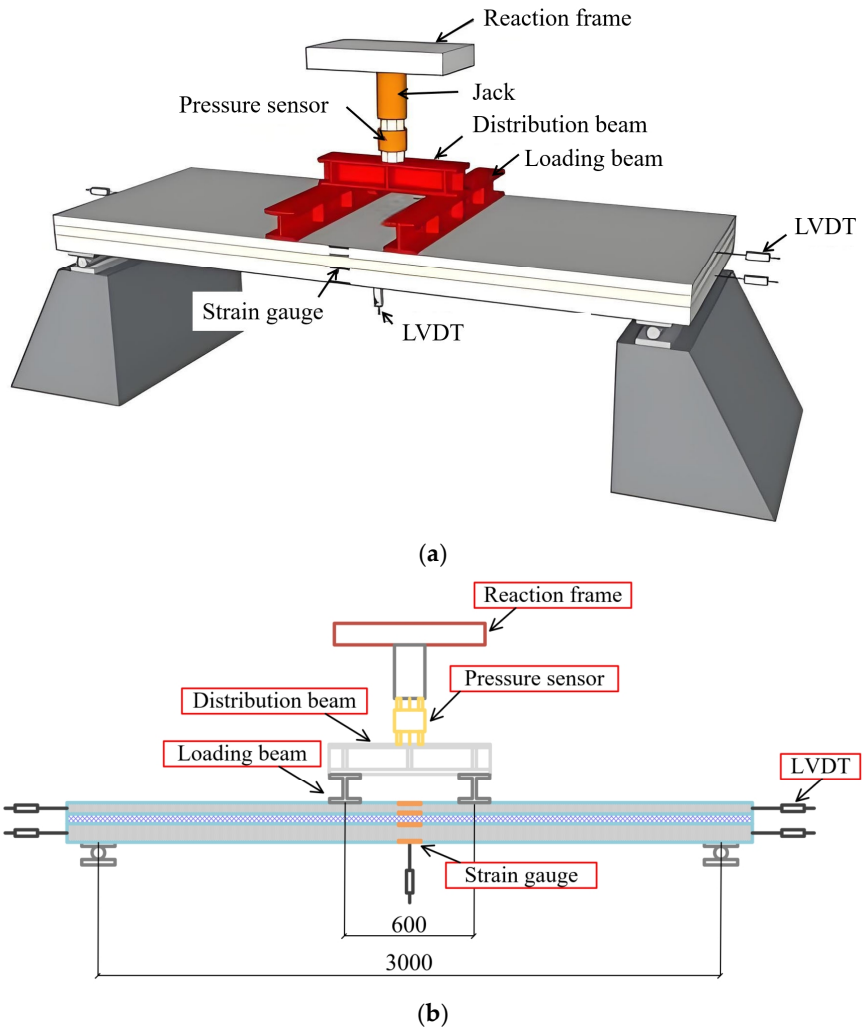


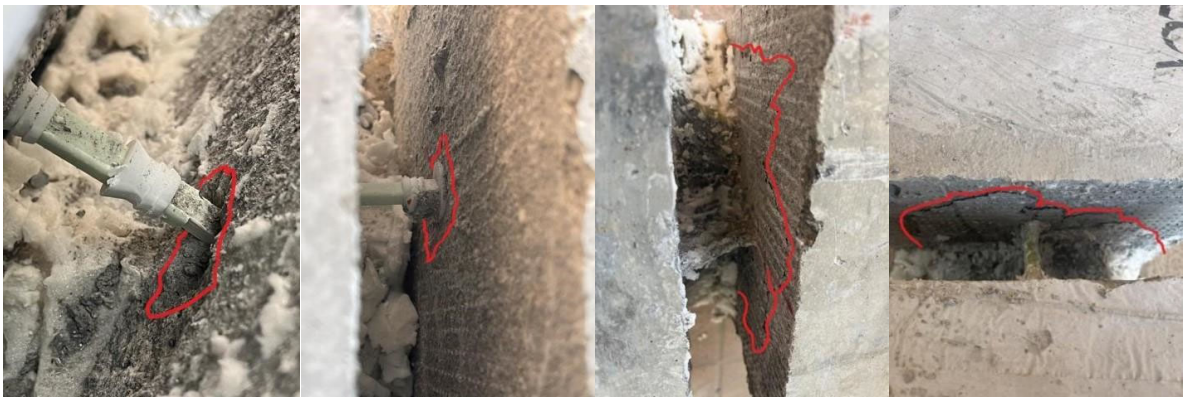
Figure 11. Test setup: (**a**) loading device 3D model diagram; (**b**) load the device main view.

3. Experimental Results and Discussion

3.1. Drawing Property

3.1.1. Drawing Failure Modes

In the initial loading stage, the POT-C bears a relatively small load and does not show significant changes. When approaching the peak load, as the relative displacement increased, the bonding surface between the insulation board and the lower concrete began to separate, and cracks rapidly developed. After continued loading, the cracks expanded and eventually, under peak load, the lower anchorage end of the connector suffered pull-out failure, as shown in Figure 12a; the main body of the connector broke, and the bearing capacity of the specimen suddenly dropped, showing brittle failure. The test ended. The failure mode of POT-R is similar to that of POT-C, with the only difference being the concrete material, which ultimately exhibits brittle failure, as shown in Figure 12b. The POG-C was made of ordinary C35 concrete, and the loading process was similar to that of POT-C. However, after the load reached its peak, the GFRP connector underwent fiber fracture, and the concrete at the anchorage end of the connector peeled off extensively. The bearing capacity of the specimen decreased to the failure load, showing ductile failure, as shown in Figure 12c. The POG-R was similar to POG-C, using fully recycled concrete. During the loading process, it experienced punching and splitting failure, and ultimately exhibited ductile failure, as shown in Figure 12d.



(**a**) (**b**) (**c**) (**d**)

Figure 12. Failure state of specimen pull-out test: (**a**) POT-C; (**b**) POT-R; (**c**) POG-C; (**d**) POG-R.

3.1.2. Displacement Under Load

To compare the tensile strengths of different connectors and concrete materials, load displacement curves of four specimens were plotted, as shown in Figure 13. From the curve, it can be seen that POT-C and POT-R using Thermomass MS-type needle connectors exhibited a cliff-like steep drop after reaching peak load, showing brittle failure. The specimens using GFRP four-footstool-type connectors experienced load fluctuations after peak load, ultimately resulting in ductile failure. The gradual deformation of GFRP under load allowed energy absorption and displacement beyond the peak, causing load fluctuations as the connector underwent progressive deformation. The cross-combination design of the connector led to localized deformations, causing stress redistribution and further load fluctuations, characteristic of ductile materials. All the specimens showed a linear increase in the stage of load rise, but during this process, the foam insulation board showed a slight steep drop when separated from the concrete.

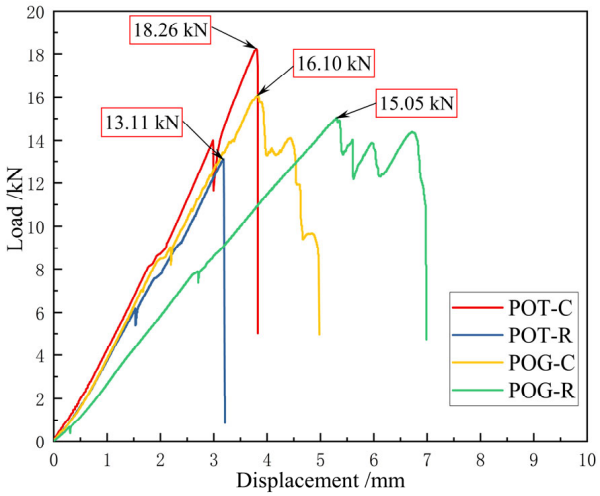


Figure 13. Load–displacement curves of specimen pull-out test.

Through comparative analysis of connectors and concrete materials, it was found that the displacement of POG-C and POG-R during tensile failure was significantly greater than that of POT-C and POT-R. In terms of ultimate tensile bearing capacity, the tensile bearing capacity of POT-C was higher than that of POG-C, while the bearing capacity of POG-R was higher than that of POT-R. Overall, C35 specimens exhibited stronger tensile strength due to their higher strength, which resulted in a tighter interaction between the connectors and the concrete.

3.2. Shear Behaviour

3.2.1. Shear Failure Modes

During the loading process of CT-C, the initial load was relatively small, and the connectors did not show significant deformation. The concrete in the insulation board area slightly cracked. As the load gradually increased, the shear bearing capacity of the connector approached its limit. With a "bang" sound, indicating fracture, obvious cracks appeared on the surface of the connector, and bending failure occurred, as shown in Figure 14a, resulting in a rapid decrease in the bearing capacity of the specimen, and ultimately brittle failure. The loading process of CT-R was similar to that of CT-C, but due to the use of fully recycled concrete, the shear force borne by the connectors caused the rapid expansion of concrete cracks in the insulation board area, and the failure modes of the connectors also manifested as shear and bending failure, as shown in Figure 14b.



(**a**) (**b**) (**c**) (**d**)

Figure 14. Failure state of specimen shear test: (**a**) CT-C; (**b**) CT-R; (**c**) CG-C; (**d**) CG-R.

During the loading process of CG-C, the behaviors of the connecting components became more complex. Firstly, the right connecting component bore a load approaching its limit, followed by the sound of the GFRP reinforcement fiber fracturing, and the connecting component showed obvious bending and fracture. As the load continued to increase, the left connector also eventually failed, with the failure modes of shear and tensile fracture, as shown in Figure 14c, indicating the brittle failure of the connector under bidirectional stress. The failure process of CG-R was similar to that of CG-C, but due to the lower compressive strength of fully recycled concrete, larger concrete crushing areas were generated in the connectors under stress, and the fibers of the connectors showed more obvious fractures and bifurcations, resulting in further increases in the failure area, as shown in Figure 14d.

3.2.2. Load-Displacement Curve

By analyzing the load displacement curve (Figure 15), it can be found that the trend of the shear failure load displacement curve was similar for specimens using the same connectors. The CT-C and CT-R of Thermomass MS-type needle connectors exhibited a unimodal state, with both connectors jointly bearing the load. After failure occurred, the specimens lost their load-bearing capacity. The CG-C and CG-R of GFRP four-footstool-type connectors exhibited a bimodal state, showing two failures. Firstly, the two connectors on the same side failed, resulting in a sudden drop in bearing capacity. Then, the connector on the other side failed, forming a second peak, and the load decreased and remained at a relatively small level. The first peak represents the elastic phase, where the connector transfers were loaded without significant deformation. After the first peak, localized plastic deformations occurred, causing a temporary reduction in load-bearing capacity. The second peak indicates force reorganization and stress redistribution, briefly restoring load capacity

before final failure. This pattern highlights the ability of the cross-combination design of the GFRP material and the connector to absorb energy and maintain load transfer despite localized failures.

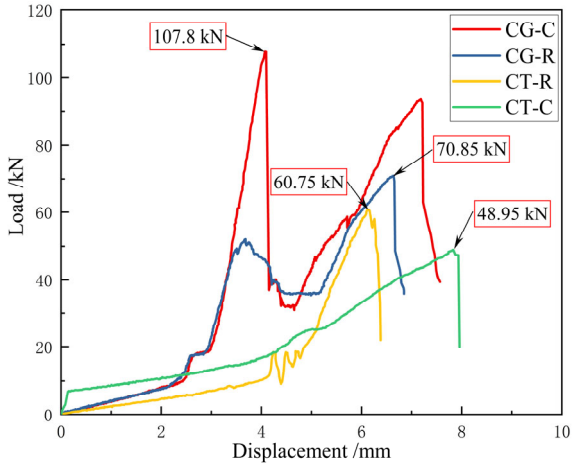


Figure 15. Load–displacement curves of each specimen shear test.

In terms of the types of connectors, specimens using GFRP four-footstool-type connectors had significantly higher shear bearing capacity than specimens using Thermomass MS-type connectors, whether in ordinary concrete or recycled concrete. The ultimate shear-bearing capacity of CG-C was 107.80 kN, which is about 1.2 times higher than that of CT-C. In the recycled concrete specimens, the ultimate shear bearing capacity of CG-R was 70.85 kN, which is 16.62% higher than that of CT-R. In addition, the displacement of GFRP four-footstool-type connectors during failure was smaller, and their comprehensive performances were better than those of Thermomass MS-type connectors. The influence of concrete type was manifested in that, when using the same connectors, the shear bearing capacity of C35 specimens was significantly higher than that of recycled concrete specimens. The main reason is that the compressive strength of C35 was higher, resulting in the higher shear strength of specimens when subjected to shear force.

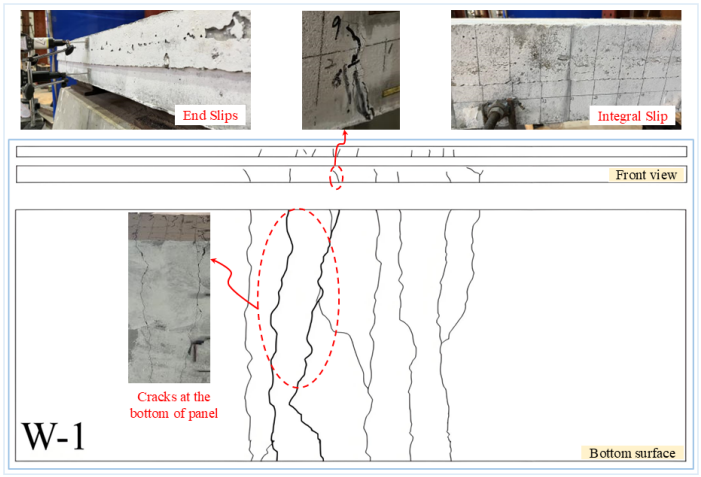
3.3. Flexural Behaviour

3.3.1. Flexural Failure Modes

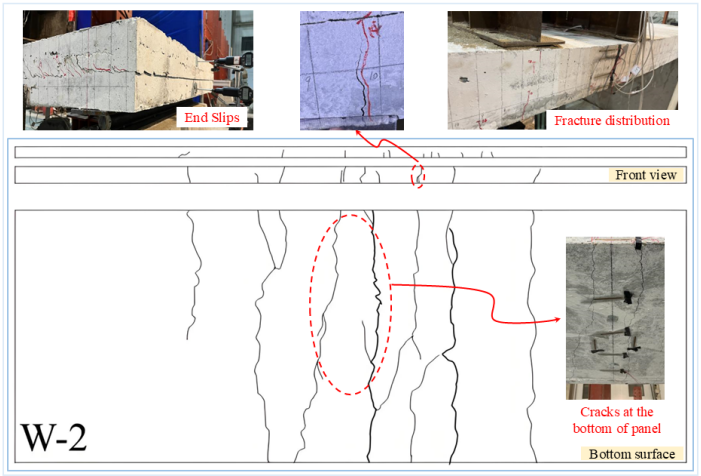
The flexural behavior results are shown in Table 9. As shown in Figure 16a, W-1 did not undergo significant damage during the initial loading stage, but when the load reached 10 kN, the specimen cracked, and a 50 mm-long crack appeared at the mid span of the specimen. As the load increased, the cracks gradually expanded. When the load reached 22 kN, new cracks appeared at the bottom of the specimen, and the mid span deflection increased sharply to 35.89 mm. When further loaded to 26 kN, the specimen entered the yielding stage, with a sharp decrease in load to 21.69 kN and a rapid increase in mid-span deflection to 62.03 mm, ultimately indicating failure. As shown in Figure 16b, W-2 showed a similar trend, but cracking occurred at a later stage, and the crack distribution was more widespread. When the load reached 34 kN, the crack width of the specimen significantly increased, and the crack extended to various areas of the specimen. When the final load reached 41.75 kN, the specimen failed. As shown in Figure 16c, the loading processes of W-3 and W-4 were relatively stable, and the crack propagation was relatively uniform. When W-3 reached the failure standard specified in the specifications, the load was 47.89 kN, and W-4 had a load of 44.73 kN at a deflection of 58 mm. W-4 showed no significant slip phenomenon throughout the entire testing process, demonstrating a good combination of inner and outer wall panel structures, as shown in Figure 16d.

Table 9. Results of flexural test.

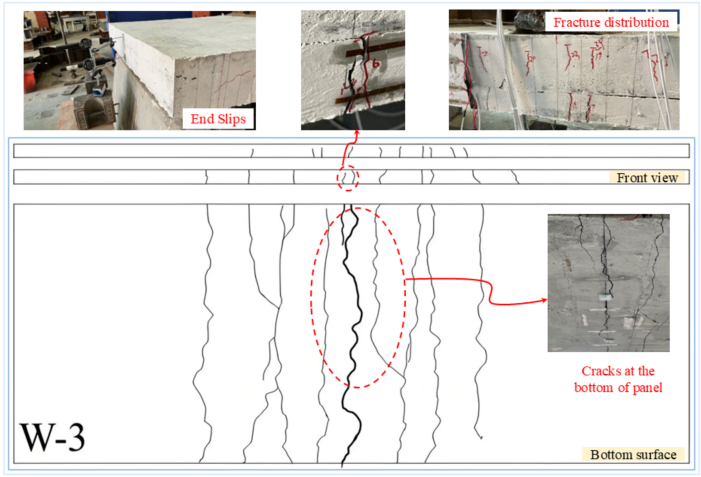
Specimen	Cracking Load/kN	Ultimate Load/kN
W-1	10.00	26.00
W-2	14.00	41.75
W-3	12.00	47.89
W-4	12.00	44.73



(**a**)

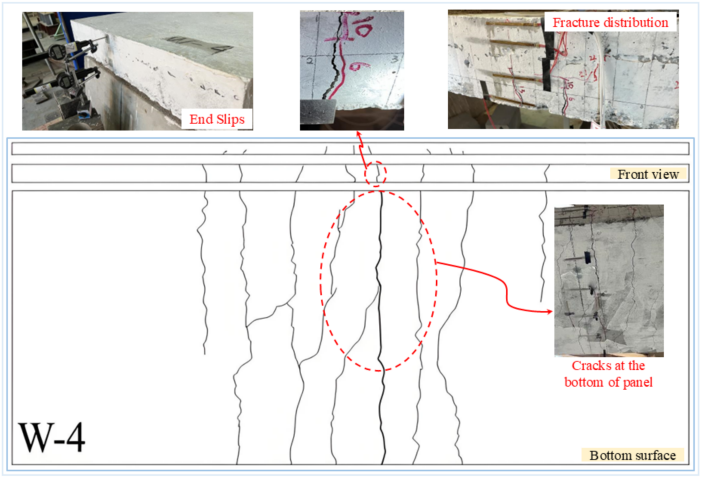


(**b**)



(**c**)

Figure 16. *Cont.*



(**d**)

Figure 16. Crack diagram of specimen bending test: (**a**) W-1; (**b**) W-2; (**c**) W-3; (**d**) W-4.

3.3.2. Cracking Behavior

As shown in Figure 16a, W-1 used a Thermomass MS-type connector, and the cracks were mainly concentrated in the middle of the bottom plate, with an average crack spacing of 15.71 cm. The main crack was located about 5 cm to the left of the mid-span, indicating that the stress on this connector was relatively concentrated. As shown in Figure 16b, the W-2 used GFRP four-footstool-type connectors, and the crack distribution was more uniform than in W-1, with an average crack spacing of 23.57 cm, an increase of 50% compared to W-1. The main crack was located about 10 cm to the right of the bottom span, indicating that GFRP four-footstool-type connectors can better disperse the stress on the bottom concrete, improving the distribution of cracks. As shown in Figure 16c, the crack spacing of W-3 was the smallest, with an average of 14.44 cm. The main crack was located in the center of the bottom plate, and the dense cracks were due to the small thickness of the bottom plate and poor crack resistance of the specimen. As shown in Figure 16d, the crack interval of W-4 was 20.63 cm, similar to W-2. The main crack was located about 15 cm to the right of the mid-span of the bottom plate, showing a relatively uniform crack distribution, indicating a more balanced stress situation.

3.3.3. Load–Mid-Span Deflection

As shown in Figure 17, the primary difference between samples W-1 and W-2 lies in the type of connector used. Sample W-1 employed ordinary concrete and Thermomass MS connectors, while W-2 utilized GFRP four-footstool connectors. The load–deflection curve for W-2 is notably higher than that for W-1, with the maximum bending capacity of W-2 being 60.58% greater than that of W-1. This indicates that GFRP four-footstool connectors provided superior shear-bearing capacity, and effectively resisted misalignment and sliding between the inner and outer wall panels, thereby enhancing the bending capacity. W-1 entered the yield stage after reaching a cracking load of 10 kN, and its curve slope decreased rapidly, while the slope of the W-2 curve remained relatively stable, delaying the yield stage. This demonstrates the advantage of GFRP four-footstool connectors in improving bending capacity.

For samples W-2 and W-4, both using GFRP four-footstool connectors, the key difference is that W-4 incorporated recycled concrete, while W-2 used ordinary concrete. The load–deflection curve for W-4 is similar to that of W-2, but the curve of W-4 shows a faster decrease in slope, suggesting that the strength of recycled concrete is lower, resulting in weaker resistance to bending loads. However, after the yielding stage, the flexural capacity

of W-4 exceeded that of W-2 by 7.14%, indicating that recycled concrete demonstrated good flexural strength under certain conditions. Overall, the mechanical properties of W-4 (with recycled concrete) were comparable to those of W-2, suggesting that the recycled content had minimal effect on the performance under the test conditions. This can be attributed to factors such as strength requirements met through processing, mix design adjustments, and similar properties between W-2 and W-4. Therefore, with appropriate optimization, recycled concrete can perform similarly to ordinary concrete.

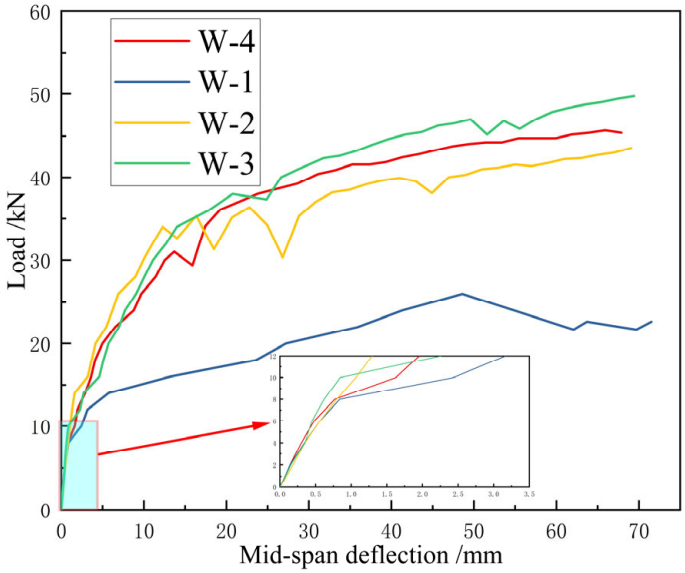


Figure 17. Load–mid-span deflection curve of specimen bending test.

In the comparison between W-3 and W-4, both of which used GFRP four-footstool connectors and recycled concrete, W-3 featured equal thicknesses for the inner and outer wall panels, whereas W-4 included a 50 mm-thick insulation board between the inner and outer panels. Although the load–displacement curves for the two samples followed a similar trend, the bending capacity of W-3 was 3.25 kN, 7.26% lower than that of W-4. This indicates that the position of the insulation board and the thickness of the wall panels significantly affected the flexural bearing capacity, with the structural configuration of W-4 demonstrating superior performance.

3.3.4. Load-Wythe Slip Responses

From the comprehensive comparison of load slip curves, as shown in Figure 18, it can be seen that samples with the same connector type exhibited similar curve shapes and changing trends. When the mid-span of the specimen reached the failure deflection, the relative slip between the inner and outer wall panels of W-1 using the Thermomass MS connector was the largest, which was 129.47% higher than that of W-2 using a GFRP four-footstool connector. This phenomenon indicates that GFRP four-footstool type connectors significantly improve the combination performance of exterior wall panels and reduce the slip between interior and exterior wall panels. In contrast, the relative slip ratio of sample W-4 increased by 81.75% compared to W-2, further demonstrating the significant influence of concrete strength on the performance of the wall panel combination. Finally, compared with sample W-4, the relative slip rate of sample W-3 only increased by 5.41%, indicating that the position of the insulation board had little effect on the performance of the wall panel combination.

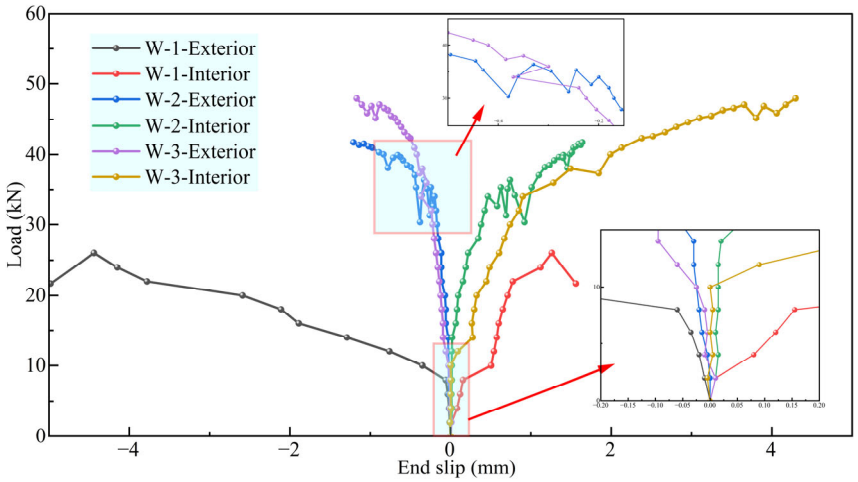


Figure 18. Load–slip curve of specimen.

3.3.5. Calculation of Combination Degree and Flexural Bearing Capacity

This section sets up equivalent models for fully composite sandwich wall panels and non-composite sandwich wall panels, and calculates the bending capacity of both models separately. By using strength calculation theory, we here determine the degree of combination of each specimen. In the model of non-composite wall panels, during the loading process of the experiment, the inner and outer walls are treated as two independent concrete slabs without interaction. The calculation model can be regarded as the superposition of the strength of two reinforced concrete slabs with different thicknesses, as shown in Figure 19.

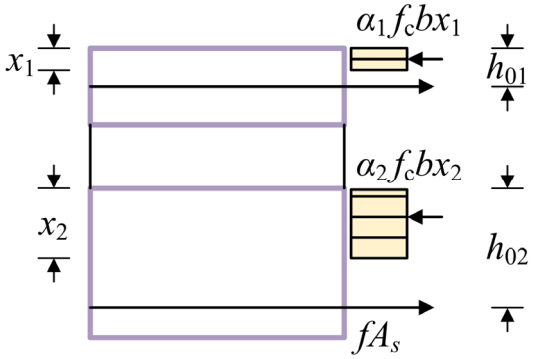


Figure 19. Non-composite wall panel calculation diagram.

According to the method specified in the "Code for Design of Concrete Structures" GB50010-2010 [36], the bending moment and load of the concrete panel of the sandwich wall panel in this test were calculated. The bending moment calculation formulas are as follows:

$$M_{nc} = M_{nc1} + M_{nc2} \quad (1)$$

$$M_{nc1} = fA_s(h_{01} - 0.5x_1) \quad (2)$$

$$M_{nc2} = fA_s(h_{02} - 0.5x_2) \quad (3)$$

where A_s is the sum of the cross-sectional areas of the tensile reinforcement, with the reinforcement distribution being consistent between the inner and outer wall panels, where A_s = 301.44 mm^2. h_0 denotes the effective height of the section, while f is the strength of the reinforcement. The yield strength standard value f_{yk} and the ultimate strength standard value f_{stk} of HRB400-grade steel bars are substituted into f, from which the yield moment

and ultimate moment of the individual concrete panel can be determined. x represents the height of the compression zone, and the specimen width b is 1200 mm.

In this experiment, the dimensions of the inner and outer wall panels of specimens W-1, W-2, and W-4 are taken as consistent. The inner wall panel has a thickness of 80 mm, and the outer wall panel has a thickness of 50 mm for calculations. The wall panel of specimen W-3 has an equal thickness for both the inner and outer panels, which is 65 mm, with the same reinforcement layout. Only one side is calculated, and the moment for W-3 is obtained by multiplying this by 2.

$$F_{nc} = \frac{8M_{nc}}{l} \tag{4}$$

The load on the fully composite wall panel is entirely transmitted through the connectors in the middle insulation layer. The two separate wall panels can be treated as a single entity under load, with no relative displacement between the panels. The calculation process is identical to that of solid slabs, as shown in Figure 20.

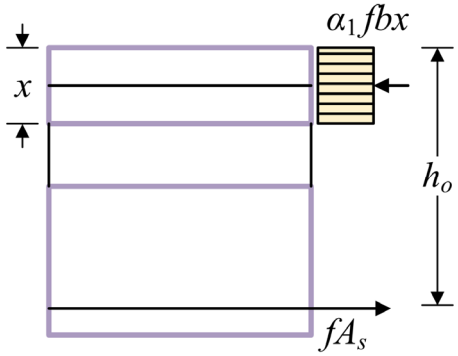


Figure 20. Completely combined wall panel calculation diagram.

Similarly, according to the calculation formula for double-reinforced cross-sections in the "Code for Design of Concrete Structures" (GB50010-2010) [36], the inner and outer wall panels are considered as a single entity and calculated using the following formula:

$$M_{fc} = fA_s(h_0 - 0.5x) \tag{5}$$

where A_s is the cross-sectional area of the tensile reinforcement; h_0 is the effective height of the section, where h_0 = 155 mm; f is the reinforcement strength. By substituting the yield strength standard value f_{yk} and the ultimate strength standard value f_{stk} of HRB400-grade steel into f, the yield moment and ultimate moment of the individual concrete panel can be determined. x is the height of the compression zone, given by $x = \frac{fA_s}{\alpha_1 f_c b}$, and b is the specimen width, which is 1200 mm.

In this experiment, the dimensions of the inner and outer wall panels of specimens W-1, W-2, and W-4 are consistent, with the inner wall panel having a thickness of 80 mm and the outer wall panel a thickness of 50 mm for calculations. For W-3, the inner and outer wall panels have equal thicknesses of 65 mm, with the same reinforcement layout. Only one side is calculated, and the moment for W-3 is obtained by multiplying this by 2. The bending moments for each wall panel are calculated separately according to their respective dimensions.

The bending capacity is then determined based on the simply supported beam four-point bending Formula (6), as follows:

$$F_{fc} = \frac{8M_{fc}}{l} \tag{6}$$

The composite degree of the wall panel is represented by the composite index κ, which is calculated according to the Formula (7). Table 10 provides the statistical results for the composite degree calculations at the yield load and ultimate load states for each experimental wall panel.

$$\kappa = \frac{F_{exp} - F_{nc}}{F_{fc} - F_{nc}} \times 100 \quad (7)$$

where F_{exp} is the experimentally measured load.

Table 10. Combination degree of wall panels.

Specimen	Yield Load/kN	Ultimate Load/kN	κ (Yield)/%	κ (Ultimate)/%
W-1	22.00	26.00	−7.14	−15.15
W-2	34.00	41.75	40.71	30.74
W-3	38.30	47.89	58.77	49.93
W-4	35.78	44.73	48.79	40.80

From the data in Table 10, it can be seen that the bonding degree between sample W-1 and the Thermomass MS connector was the lowest. In contrast, the adhesion between sample W-2 and the GFRP four-footstool connector reached 40.71% under yield load and 30.74% under ultimate load, which values are 47.85% and 45.89% higher than those of W-1, respectively. This difference is mainly due to the fact that during the bending process of the specimen, the part between the loading points was a pure bending section, and there was significant friction between the outer side of the loading point and the supporting ends of the inner and outer wall panels, resulting in higher shear forces on the connecting components. Due to the stronger shear strength of the GFRP four-footstool connector compared to the Thermomass MS connector, the bonding degree of W-2 was higher. Sample W-3 had the highest degree of combination, with the same thicknesses of inner and outer wall panels. During the bending process, the concrete structure with thicker upper outer wall panels could withstand greater pressure, thus achieving the strongest bonding effect.

3.3.6. Modification of Flexural Strength Calculation

Due to the differences in the types and structural forms of connectors used for exterior wall cladding, as well as their varying degrees of combination, the calculation of bending capacity becomes relatively complex. To simplify the calculation, this section proposes a correction factor for the flexural strength of GFRP four-footstool-type connectors for exterior wall cladding, in order to facilitate the calculation of flexural strength. Based on the comparison between the bending strength calculated by the fully combined model in the previous section and the measured strength, the correction factor has here been determined. The specific data are shown in Table 11.

Table 11. Correction value for flexural strength calculation of wall panels.

Specimen	Experimental Flexural Strength F_G/kN	Calculation of Flexural Strength F_{fc}/kN	Correction Factor/γ	Correction Value/Test Value
W-2	41.75	65.52	0.68	1.07
W-3	47.89	65.22	0.68	0.93
W-4	44.73	65.22	0.68	0.99

From the results in Table 11, it can be seen that when calculating the flexural strength of GFRP four-footstool connector wall panels, the flexural bearing capacity can first be calculated based on the calculation Formulas (5) and (6) of the fully composite wall panel model. Next, one must multiply the calculation result by the combination degree reduction factor γ = 0.68 to obtain the corrected flexural strength. The revised calculation formula is shown in Formula (8), and the deviation between the bending capacity calculated using this method and the measured value is small, making the calculation process more convenient.

$$F_G = \gamma \cdot \frac{8M_{fc}}{l} \tag{8}$$

4. Conclusions

This article proposes a new type of GFRP four-footstool connector and combines it with a common Thermomass MS needle connector to conduct experimental research on the pull-out, shear, and full-size wall panel bending performance of prefabricated insulation exterior wall panels made of fully recycled concrete and ordinary C35 concrete. Through experimental analysis, the following conclusions can be drawn.

The pull-out test revealed significant differences in the failure modes of two types of connectors. The specimen using the Thermomass MS connector exhibited brittle failure under the ultimate load, while the specimen with the GFRP four-footstool connector demonstrated enhanced ductility. These specimens showed greater relative displacement and a larger safety margin before failure, ultimately undergoing a ductile failure mode. Notably, the tensile strength of samples using recycled concrete increased by 14.8% compared to ordinary concrete, highlighting the positive impact of recycled materials on performance.

In the shear test, the Thermomass MS connector failed due to the connector itself, while samples made of both ordinary concrete and fully recycled concrete failed due to bending when the connector reached its maximum capacity. In contrast, the specimens with GFRP four-footstool connectors exhibited more complex failure behavior, including damage to the connector material and crushing of the concrete in the compression zone. Among all the samples, the one with the GFRP four-footstool connector demonstrated the highest ultimate shear bearing capacity.

In the bending test, crack formation in the specimen with the Thermomass MS connector was concentrated in the central area, while the sample with the GFRP four-footstool connector showed a 50% increase in crack spacing, indicating an improvement in crack distribution. The sample with the GFRP four-footstool connector exhibited a more uniform crack pattern and a wider stress range, with its maximum bending capacity being 60.58% higher than that of the Thermomass MS connector. The difference in failure mode and bearing capacity between the ordinary concrete and recycled concrete specimens was minimal, indicating that the GFRP four-footstool connector performed similarly to the joint action of both concrete types.

A comparative analysis of specimens with varying thicknesses of inner and outer wall panels revealed the influence of insulation board placement on bending performance. Although the early load–deflection curves were similar, the flexural capacity of specimens with equal concrete thickness on both sides of the insulation board was 7.26% higher than that of specimens with unequal thicknesses. This suggests that the positioning of the insulation layer affects the structural behavior of the wall panel, with the insulation layer ideally placed at the center during design.

Compared to the Thermomass MS connector sample, the relative slip observed in the specimen using the GFRP four-footstool connector increased significantly by 129.47%, highlighting the role of the GFRP connector in enhancing the overall connection between components. This finding emphasizes the importance of selecting appropriate connector

types to improve the performance of prefabricated wall panels. To simplify design calculations, a reduction factor (γ) for the combination degree of GFRP four-footstool connectors is proposed, offering a practical approach for future design considerations.

Author Contributions: Methodology, X.L.; Software, X.L.; Validation, X.L., H.S. and T.Z.; Formal analysis, X.L.; Investigation, X.L., H.S., T.Z., T.B., H.Y., J.S. and H.F.; Resources, X.L.; Data curation, X.L.; Writing—original draft, H.S. and T.Z.; Writing—review & editing, X.L. and H.F.; Visualization, X.L.; Supervision, X.L.; Project administration, X.L.; Funding acquisition, X.L. All authors have read and agreed to the published version of the manuscript.

Funding: This research was funded by the National Natural Science Foundation of China [grant No. 52278507]; the Natural Science Foundation of Shandong Province [grant No. ZR2020ME245]; and the Major Scientific & Technological Innovation Project of Shandong Province [grant No. 2021CXGC011204].

Data Availability Statement: The original contributions presented in this study are included in the article. Further inquiries can be directed to the corresponding author.

Conflicts of Interest: The authors declare that we have no known competing financial interests or personal relationships that could have appeared to influence the work reported in this paper.

References

1. Ding, X.; Yu, J.; Lin, J.; Chen, Z.; Li, J. Experimental investigations of prefabricated lightweight self-insulating foamed concrete wall panels. *Structures* **2024**, *61*, 106001. [CrossRef]
2. Palani, H.; Karatas, A. Investigating the disparities between experimental and computational analyses of thermal performance in prefabricated wall panels. *Appl. Therm. Eng.* **2024**, *236*, 121568. [CrossRef]
3. Yu, S.; Liu, Y.; Wang, D.; Bahaj, A.; Wu, Y.; Liu, J. Review of thermal and environmental performance of prefabricated buildings: Implications to emission reductions in China. *Renew. Sustain. Energy Rev.* **2021**, *137*, 110472. [CrossRef]
4. Tawil, H.; Tan, C.G.; Sulong, N.H.R.; Nazri, F.M.; Sherif, M.M.; El-Shafie, A. Mechanical and Thermal Properties of Composite Precast Concrete Sandwich Panels: A Review. *Buildings* **2022**, *12*, 1429. [CrossRef]
5. Oliveira, T.; Carvalho, J.; Mendes, J.; Souza, G.; Carvalho, V.; Peixoto, R. Precast concrete sandwich panels (PCSP): An analytical review and evaluation of CO_2 equivalent. *Constr. Build. Mater.* **2022**, *358*, 129424. [CrossRef]
6. Tushar, Q.; Zhang, G.; Bhuiyan, M.A.; Navaratnam, S.; Giustozzi, F.; Hou, L. Retrofit of Building Façade Using Precast Sandwich Panel: An Integrated Thermal and Environmental Assessment on BIM-Based LCA. *Buildings* **2022**, *12*, 2098. [CrossRef]
7. Ghazy, M.F.; Abd Elaty, M.A.A.; Sakr, M.A.E.; Arafa, E.M. Thermo-Mechanical Performance of Sustainable Lightweight Sandwich Panels Utilizing Ultra-High-Performance Fiber-Reinforced Concrete. *Buildings* **2025**, *15*, 593. [CrossRef]
8. Zou, J.; Cao, B.; Zeng, X.; Zhang, Y. Lateral Performance of Composite Wall with Cold-Formed Thin-Walled Steel–Concrete Sandwich Panel. *Buildings* **2024**, *14*, 2928. [CrossRef]
9. Alves, L.F.; Pessôa, P.d.M.; Jardim, P.I.L.G.; Faustino, E.; dos Santos, H.F.; Lahr, F.A.R.; de Almeida, D.H.; Christoforo, A.L. Numerical Evaluation of the Influence of Using Carbon-Fiber-Reinforced Polymer Rebars as Shear Connectors for Cross-Laminated Timber–Concrete Panels. *Buildings* **2024**, *14*, 2178. [CrossRef]
10. Jiang, H.; Xie, L.; Chang, F.; Cao, Y.; Guo, Z. Study on the Composite Performance of Sandwich Wall Panels with SGCCs. *Buildings* **2025**, *15*, 65. [CrossRef]
11. Wang, X.; Sun, H.; Hou, Y.; Li, Y. Study on Seismic Performance of Steel Frame Installed New-Type Lightweight Concrete Composite Exterior Wallboard. *Buildings* **2024**, *14*, 2224. [CrossRef]
12. Silva, J.K.F.; Lameiras, R.d.M. Experimental Analysis of the Mechanical Behavior of Shear Connectors for Precast Sandwich Wall Panels When Subjected to the Push-Out Tests. *Buildings* **2024**, *14*, 3246. [CrossRef]
13. Barbosa, K.; Silva, W.T.M.; Silva, R.; Vital, W.; Bezerra, L.M. Experimental Investigation of Axially Loaded Precast Sandwich Panels. *Buildings* **2023**, *13*, 1993. [CrossRef]
14. Sevil Yaman, T.; Lucier, G. Shear Transfer Mechanism between CFRP Grid and EPS Rigid Foam Insulation of Precast Concrete Sandwich Panels. *Buildings* **2023**, *13*, 928. [CrossRef]
15. Liu, X.; Wang, X.; Yang, T.; Wu, Z. The Shear Behavior of Insulated Precast Concrete Sandwich Panels Reinforced with BFRP. *Buildings* **2022**, *12*, 1326. [CrossRef]
16. Lou, X.; Xue, W.; Bai, H.; Li, Y.; Huang, Q. Shear behavior of stainless-steel plate connectors for insulated precast concrete sandwich panels. *Structures* **2022**, *44*, 1046–1056. [CrossRef]

17. Zhao, M.; Chong, X.; Huang, J.-Q.; Jiang, Q.; Feng, Y.-L.; Chang, Y. Experimental and numerical investigations on the axial compression performance of precast geopolymer concrete sandwich wall panel. *J. Build. Eng.* **2024**, *95*, 110303. [CrossRef]
18. O'Hegarty, R.; Kinnane, O. Review of precast concrete sandwich panels and their innovations. *Constr. Build. Mater.* **2020**, *233*, 117145. [CrossRef]
19. Bian, Y.; Xiong, F.; Liu, Y.; Ge, Q. Flexural performance of novel ECC-RC composite sandwich panels. *Eng. Struct.* **2023**, *292*, 116547. [CrossRef]
20. Huang, J.-Q.; Dai, J.-G. Flexural performance of precast geopolymer concrete sandwich panel enabled by FRP connector. *Compos. Struct.* **2020**, *248*, 112563. [CrossRef]
21. Kim, J.; You, Y.-C. Composite Behavior of a Novel Insulated Concrete Sandwich Wall Panel Reinforced with GFRP Shear Grids: Effects of Insulation Types. *Materials* **2015**, *8*, 899–913. [CrossRef] [PubMed]
22. Wang, L.; Wu, Z.; Liu, W.; Wan, L. Structural behavior of load-bearing sandwich wall panels with GFRP skin and a foam-web core. *Sci. Eng. Compos. Mater.* **2018**, *25*, 173–188. [CrossRef]
23. Choi, I.; Kim, J.; You, Y. Effect of cyclic loading on composite behavior of insulated concrete sandwich wall panels with GFRP shear connectors. *Compos. Part B Eng.* **2016**, *96*, 7–19. [CrossRef]
24. Benayoune, A.; Abdul, S.; Trikha, D.; Ali, A.A.; Ellinna, S.H.M. Flexural behaviour of pre-cast concrete sandwich composite panel-Experimental and theoretical investigations. *Constr. Build. Mater.* **2008**, *22*, 580–592. [CrossRef]
25. Sharaf, T.; Shawkat, W.; Fam, A. Structural Performance of Sandwich Wall Panels with Different Foam Core Densities in One-way Bending. *J. Compos. Mater.* **2010**, *44*, 2249–2263. [CrossRef]
26. Zhi, Q.; Guo, Z. Experimental evaluation of precast concrete sandwich wall panels with steel–glass fiber–reinforced polymer shear connectors. *Adv. Struct. Eng.* **2017**, *20*, 1476–1492. [CrossRef]
27. Naito, C.; Hoemann, J.; Beacraft, M.; Bewick, B. Performance and Characterization of Shear Ties for Use in Insulated Precast Concrete Sandwich Wall Panels. *J. Struct. Eng.* **2012**, *138*, 52–61. [CrossRef]
28. Kang, W.; Kim, J. Reliability-based flexural design models for concrete sandwich wall panels with continuous GFRP shear connectors. *Compos. Part B Eng.* **2016**, *89*, 340–351. [CrossRef]
29. Xiong, F.; Bian, Y.; Liu, Y.; Ge, Q.; Deng, C. Data-driven prediction method for flexural performance of ECC composite sandwich panels. *Structures* **2024**, *70*, 107524. [CrossRef]
30. He, J.; Xu, Z.; Zhang, L.; Lin, Z.; Hu, Z.; Li, Q.; Dong, Y. Shaking table tests and seismic assessment of a full-scale precast concrete sandwich wall panel structure with bolt connections. *Eng. Struct.* **2023**, *278*, 115543. [CrossRef]
31. Choi, W.; Jang, S.; Yun, H. Design properties of insulated precast concrete sandwich panels with composite shear connectors. *Compos. Part B Eng.* **2019**, *157*, 36–42. [CrossRef]
32. Zhang, M.; Feng, W.; Chen, K.; Li, B. Flexural Behavior of a New Precast Insulation Mortar Sandwich Panel. *Appl. Sci.* **2024**, *14*, 2071. [CrossRef]
33. Zhao, K.; Fan, Z.; Zhang, Y.; Xu, Y.; Liu, S. Experimental Study on Seismic Performance of Prefabricated Monolithic Concrete–Polystyrene Panel Composite Wall Panels. *Buildings* **2024**, *14*, 442. [CrossRef]
34. Chen, D.; Li, K.; Yuan, Z.; Cheng, B.; Kang, X. Shear Behavior of FRP Connectors in Precast Sandwich Insulation Wall Panels. *Buildings* **2022**, *12*, 1095. [CrossRef]
35. Xie, J.; Chen, F.; Zhao, J.; Lu, P.; Liu, F.; Li, L. Flexural behaviour of full-scale precast recycled concrete sandwich panels with BFRP connectors. *J. Build. Eng.* **2022**, *56*, 104816. [CrossRef]
36. *GB 50010-2010*; Chinese Standard Code for Design of Concrete Structures. China Architecture & Building Press: Beijing, China, 2015.

Disclaimer/Publisher's Note: The statements, opinions and data contained in all publications are solely those of the individual author(s) and contributor(s) and not of MDPI and/or the editor(s). MDPI and/or the editor(s) disclaim responsibility for any injury to people or property resulting from any ideas, methods, instructions or products referred to in the content.